Tumor margin assessment of surgical tissue specimen of cancer patients using label-free hyperspectral imaging

Baowei Fei, *Emory University*
Guolan Lu, *Georgia Institute of Technology*
Xu Wang, *Emory University*
Hongzheng Zhang, *Emory University*
James Little III, *Emory University*
Kelly Magliocca, *Emory University*
Amy Chen, *Emory University*

Journal Title: Proceedings of SPIE
Volume: Volume 10054
Publisher: Society of Photo-optical Instrumentation Engineers (SPIE) | 2017-01-01
Type of Work: Article | Post-print: After Peer Review
Publisher DOI: 10.1117/12.2249803
Permanent URL: https://pid.emory.edu/ark:/25593/txpm7

Final published version: http://dx.doi.org/10.1117/12.2249803

HHS Public Access

Author manuscript

Proc SPIE Int Soc Opt Eng. Author manuscript; available in PMC 2018 October 03.

Published in final edited form as:

Proc SPIE Int Soc Opt Eng. 2017 ; 10054: . doi:10.1117/12.2249803.

Tumor margin assessment of surgical tissue specimen of cancer patients using label-free hyperspectral imaging

Baowei Fei[a,b,c,d], **Guolan Lu**[b], **Xu Wang**[e], **Hongzheng Zhang**[e], **James V. Little**[f], **Kelly R. Magliocca**[f], and **Amy Y. Chen**[e]

[a]Department of Radiology and Imaging Sciences, Emory University, Atlanta, GA

[b]Department of Biomedical Engineering, Georgia Institute of Technology and Emory University

[c]Department of Mathematics & Computer Science, Emory University, Atlanta, GA

[d]Winship Cancer Institute of Emory University, Atlanta, GA

[e]Department of Otolaryngology, Emory University, Atlanta, GA

[f]Department of Pathology and Laboratory Medicine, Emory University, Atlanta, GA

Abstract

We are developing label-free hyperspectral imaging (HSI) for tumor margin assessment. HSI data, hypercube (x,y,λ), consists of a series of high-resolution images of the same field of view that are acquired at different wavelengths. Every pixel on the HSI image has an optical spectrum. We developed preprocessing and classification methods for HSI data. We used spectral features from HSI data for the classification of cancer and benign tissue. We collected surgical tissue specimens from 16 human patients who underwent head and neck (H&N) cancer surgery. We acquired both HSI, autofluorescence images, and fluorescence images with 2-NBDG and proflavine from the specimens. Digitized histologic slides were examined by an H&N pathologist. The hyperspectral imaging and classification method was able to distinguish between cancer and normal tissue from oral cavity with an average accuracy of 90±8%, sensitivity of 89±9%, and specificity of 91±6%. For tissue specimens from the thyroid, the method achieved an average accuracy of 94±6%, sensitivity of 94±6%, and specificity of 95±6%. Hyperspectral imaging outperformed autofluorescence imaging or fluorescence imaging with vital dye (2-NBDG or proflavine). This study suggests that label-free hyperspectral imaging has great potential for tumor margin assessment in surgical tissue specimens of H&N cancer patients. Further development of the hyperspectral imaging technology is warranted for its application in image-guided surgery.

Keywords

Hyperspectral imaging; image-guided surgery; tumor margin assessment; cancer detection; image classification; image quantification; head and neck cancer; label free; fluorescence imaging

Corresponding author: Baowei Fei , bfei@emory.edu, Website: https://fei-lab.org/baowei-fei/.

1. INTRODUCTION

Of the 15.2 million new cases of cancer in 2015, over 80% of cases will need surgery, some several times [1]. Surgery cures approximately 45% of all patients with cancer [2, 3]. To cure a cancer patient by surgery, the surgeon must remove the entire tumor at the time of surgery. Unfortunately, up to 39% of patients who undergo surgery leave the operating room without a complete resection due to positive or close margins [2, 4, 5]. It has been reported that a complete resection is the single most important predictor of patient survival for almost all solid cancers [6]. In breast, head & neck, lung, colon, and pancreatic cancers, complete resection is associated with a 3–5 fold improvement in survival compared to a partial or incomplete resection [7–10].

Various methods have been developed for cancer margin assessment. Visual appearance and palpation are often used by a surgeon to differentiate between malignant and benign tissue [11]. However, this visual assessment is subjective. Intra-operative frozen margin evaluation is commonly used to optimize surgical margin delineation at initial surgery [12]. Small samples from the surgical bed are selected to evaluate presence or absence of residual cancer [13]. However, intraoperative frozen section diagnosis may suffer from errors that occur during sampling and histological interpretation. In addition, histological processing can take time [14], which is labor intensive and prolongs surgery time. Fluorescence-guided imaging to navigate cancer resection has been shown to improve the number of complete resections and progression free survival [15–21]. In most cases, fluorescence-based approaches require the injection of a fluorescence contrast agent. There are clinical needs to develop label-free imaging technology and quantification methods to aid decision making during image-guided surgery.

Hyperspectral imaging, also called imaging spectrometer [22], was originated from remote sensing and has been explored for various applications by NASA [23]. With the advantages of acquiring two dimensional images across a wide range of electromagnetic spectra, HSI has been applied to numerous areas including archaeology and art conservation [24] [25], vegetation and water resource control [26] [27], food quality and safety control [28] [29], forensic medicine [30] [31], crime scene detection [32] [33], and biomedical area [34] [35].

Hyperspectral imaging has been emerged as a relatively new imaging modality for medical applications. This label-free imaging technology does not require a contrast agent and offers great potential for objective assessment of cancer margins. Light delivered to the biological tissue undergoes multiple scattering from inhomogeneity of biological structures and absorption primarily in hemoglobin, melanin and water as it propagates through tissue [36] [37]. The absorption, fluorescence and scattering characteristics of tissue change with the progression of diseases [38]. Therefore, the reflected, fluorescent and transmitted lights from tissue, where are captured by HSI, carry quantitative diagnostic information about tissue pathology [39] [40] [38, 41]. Spatially resolved spectra obtained by HSI provide diagnostic information about the tissue physiology, morphology, and composition. Recent advancements of hyperspectral cameras, image analysis methods and computational power make it possible for many exciting applications of hyperspectral imaging, such as cancer detection and image-guided surgery [42].

In this study, we developed a pipeline of preprocessing and quantification tools for hyperspectral image data. We developed image classification methods to differentiate tumor from benign tissue. We evaluated the hyperspectral imaging and classification method in surgical tissue specimens from human patients undergoing cancer surgery.

2. METHODS AND MATERIALS

2.1 Hyperspectral imaging system

A Maestro (PerkinElmer Inc., Waltham, MA) imaging system was used to acquire hyperspectral dataset. This is a wavelength-scanning system consisting of a Xenon light source, a solid-state liquid crystal filter and a 12-bit high-resolution charge-coupled device (CCD). Details about this system has been described in previous papers [43] [44]. This system is capable of obtaining reflectance images over the range of 450 nm – 950 nm with 2 nm increment, as well as fluorescence images under different excitation light sources [45].

2.2 Surgical specimen collection

Head and neck cancer patients who underwent surgery at Emory University Hospitals Midtown were recruited into the study. All tissues were collected under the clinical protocol approved by the Institutional Review Board of Emory University. During surgery, fresh surgical specimens were collected and sent to pathology for cancer assessment. Three tissue samples, *i.e., i)* clinically visible tumor, *ii)* surrounding normal tissue, and *iii)* tumor with adjacent normal tissue, were collected from the main specimen of each consented subject.

2.3 Hyperspectral image acquisition

Fresh surgical specimen were scanned with hyperspectral imaging in the following steps: *1)* Acquire white and dark reference hypercube before tissue imaging. White reference image cubes are acquired by placing a standard white reference board in the field of view. The dark reference cubes are acquired by keeping the camera shutter closed. *2)* Acquire reflectance hyperspectral images of the specimen from 450–900 nm with 5 nm intervals. *3)* Acquire fluorescence imaging with 2-NBDG (Cayman Chemical, Ann Arbor, Michigan) by incubating tissue as described in [46]. *4)* Acquire florescence imaging with proflavine (Sigma Aldrich, St. Louis, MO) similarly as described in Step *3)*.

2.4 Histological processing and analysis

After imaging, the resected specimen were fixed in formalin overnight and then sent to pathology for the standard histologic processing with hematoxylin and eosin (H&E) staining. The pathologic slides were digitally scanned, and an experienced pathologist outlined the tumor border on the digitized images for validation.

2.5 Hyperspectral data normalization

The purpose of data normalization was to remove the spectral non-uniformity of the illumination device and the influence of dark current. The raw data is normalized using the following equation:

$$I_{reflect}(\lambda) = \frac{I_{raw}(\lambda) - I_{dark}(\lambda)}{I_{white}(\lambda) - I_{dark}(\lambda)}$$

Where $I_{refelct}(\lambda)$ is the calculated normalized reflectance value at the wavelength λ. $I_{raw}(\lambda)$ is the intensity value of the sample pixel. $I_{white}(\lambda)$ and $I_{dark}(\lambda)$ are the corresponding pixel intensities from the white and dark reference images at the wavelength λ.

2.6 Glare detection and removal

Glare regions are formed due to specular reflection from the moist tissue surface and do not contain useful diagnostic information of the tissue. As we reported in [47], the glare detection method includes the following steps: 1) Estimate the first-order derivatives of spectral curves with a forward difference method; 2) Calculate the standard deviation (SD) of each derivative curve and generate an SD image for each hypercube. Glare pixels show higher SD than normal pixels. 3) Compute the intensity histogram of each SD image, fit the histogram with a loglogistic distribution, and then experimentally identify a threshold that separates glare and non-glare pixels.

2.7 Hyperspectral image classification

We analyze the spectral data to classify each pixel into normal and cancer tissue. To reduce computational time without reducing accuracy, spectral curves were averaged in non-overlapping blocks of 5× 5 to yield a spectral signature per block. All of the spectral information available in the hyperspectral data was utilized. Blocks containing glare pixels were excluded from classification process. Each block was assigned a label as cancerous or normal. We implemented ensemble linear discriminant analysis (LDA) as the classifier using MATLAB (MathWorks, Natick, MA) [48].

2.8 Pathological validation

We used the pathologic images of the same surgical specimen to validate the cancer detection with hyperspectral image classification. On the digitized H&E-stained pathological slides, the tumor margin was outlined by an H&N pathologist. To reasonably assess the performance of the classification, we chose the regions of interest (ROIs), where the tumor or normal tissue were histopathologically confirmed by the pathologist, for quantitative analysis and validation.

2.9 Performance metric

The sensitivity and specificity of the classifiers for each patient were calculated based on the number of correctly classified tumor and normal pixels/blocks of all the specimens belonging to this patient. Furthermore, we calculated how many normal pixels/blocks were correctly classified for a normal specimen, how many tumor pixels/blocks were correctly classified for a tumor specimen, as well as the sensitivity and specificity on a tumor-normal interface specimen for each patient. We evaluated the performance of the hyperspectral image classification using the areas under the curve (AUC), accuracy, sensitivity, and

specificity, as defined in the following equations (TN: true negative, TP: true positive, FP: false positive, FN: false negative):

$$\text{Accuracy}=\frac{TP+TN}{TP+FP+FN+TN};$$
$$\text{Sensitivity}=\frac{TP}{TP+FN};\ \text{Specificity}=\frac{TN}{TN+FP};$$

3. RESULTS

Fresh surgical tissue specimens were collected from 16 head and neck cancer patients. These patients included 7 oral cancer, 1 maxillary sinus cancer, 5 thyroid cancer, 1 parotid cancer, and 2 larynx cancer. As described above, we collected three types of tissue specimens from each human subject, which include: *i)* Clinically visible tumor tissue without necrosis, *ii)* Normal tissue, and *iii)* Tumor with adjacent normal tissue at the tumor-normal interface. Figure 1 shows the three tissue specimens and their corresponding histological sides.

For each patient, we used the images of the tumor and normal tissue to train the classification algorithms and then used the tumor with adjacent normal tissue to test the performance of the classification methods. In another word, the classification method built the training model with the spectral features extracted from the tumor and normal tissue and was then evaluated on the tumor-normal interface tissue of the same patient. Using the reflectance spectra from hyperspectral imaging, the hyperspectral imaging method was able to distinguish between cancer and normal tissue of the oral cavity with an average accuracy of 90±8%, sensitivity of 89±9%, and specificity of 91±6%. For tissue specimens from the thyroid, the method achieved an average accuracy of 94±6%, sensitivity of 94±6%, and specificity of 95±6%. As shown in Table 1, hyperspectral imaging outperformed autofluorescence imaging, 2-NBDG and proflavine fluorescence imaging for both cancer sites.

Figure 2 shows the photographs of the tumor and normal tissue as well as the tumor with adjacent normal tissue for a typical case. The three types of tissue demonstrate different spectral curves. The tumor margin as assessed by the classification method was close to that of the histological image outlined by the pathologist.

4. DISCUSSION

In this study, we reported automated tissue classification methods that use the spectra from 450 to 900 nm to extract diagnostic information. Each hyperspectral image contains over 2 million reflectance spectral signatures. The reflectance spectra capture the alteration of absorption and scattering properties of the tissue associated with malignant transformation. Molecular fingerprinting based on inverse modeling of reflectance spectra may shed new light on our understanding of cancer biology.

Although frozen section diagnosis is commonly used to guide surgical resection during surgery, it only samples a small portion of tissue in the resection area, which may lead to underestimation and does not guarantee margin negative resection. Moreover, this procedure

is time-consuming and labor-intensive. HSI is a wide-field imaging modality that can cove a large field of view, thus can provide rapid assessment of complete resection margins.

In this surgical specimen study, the label-free hyperspectral imaging is superior to autofluorescence imaging or fluorescence imaging with vital dye (2-NBDG or proflavine) for the detection of head and head cancer. A recent study has shown that wide-field fluorescence imaging with 2-NBDG can accurately distinguish the pathologically normal and abnormal biopsy tissue of head and neck cancer patients [49]. Proflavine has also been applied for distinguishing between benign and neoplastic mucosa in the head and neck [50]. We previously demonstrated the utility of hyperspectral imaging for head and neck cancer detection in a subcutaneous cancer animal model [47, 51] and a chemically-induced oral cancer model [52]. One prominent advantage of hyperspectral imaging is that it does not require the use of an exogenous contrast agent. Therefore, this noninvasive imaging technology can be rapidly translated from *ex vivo* tissue specimens to *in vivo* human studies, such as clinical trials of hyperspectral image-guided surgery.

5. CONCLUSION

Hyperspectral imaging is an emerging imaging modality for medical applications. This label-free imaging technology does not require a contrast agent and offers great potential for cancer detection and image-guided surgery. Hyperspectral big data contain both spatial and spectral information. Our hyperspectral image quantification tools are able to distinguish cancer from normal tissue in fresh surgical specimens of head and neck cancer patients. Further development of the hyperspectral imaging technology is warranted for its application in image-guided surgery.

ACKNOWLEDGEMENT

This research is supported in part by NIH grants (CA176684, R01CA156775, and CA204254) and by Developmental Funds from the Winship Cancer Institute of Emory University under award number P30CA138292.

REFERENCES

[1]. Sullivan R, Alatise OI, Anderson BO et al., “Global cancer surgery: delivering safe, affordable, and timely cancer surgery,” Lancet Oncol, 16(11), 1193–224 (2015). [PubMed: 26427363]

[2]. Singhal S, Nie SM, and Wang MD, [Nanotechnology Applications in Surgical Oncology], (2010).

[3]. De Grand AM, and Frangioni JV, “An operational near-infrared fluorescence imaging system prototype for large animal surgery,” Technology in Cancer Research & Treatment, 2(6), 553–562 (2003). [PubMed: 14640766]

[4]. Vaidya A, Hawke C, Tiguert R et al., “Intraoperative T staging in radical retropubic prostatectomy: is it reliable?,” Urology, 57(5), 949–54 (2001). [PubMed: 11337301]

[5]. Nguyen QT, and Tsien RY, “Fluorescence-guided surgery with live molecular navigation - a new cutting edge,” Nat Rev Cancer, 13(9), 653–62 (2013). [PubMed: 23924645]

[6]. Gebitekin C, Gupta N, Satur C et al., “Fate of patients with residual tumour at the bronchial resection margin,” European journal of cardio-thoracic surgery, 8(7), 339 (1994). [PubMed: 7946410]

[7]. Meric F, Mirza NQ, Vlastos G et al., “Positive surgical margins and ipsilateral breast tumor recurrence predict disease-specific survival after breast-conserving therapy,” Cancer, 97(4), 926–933 (2003). [PubMed: 12569592]

[8]. Sienel W, Stremmel C, Kirschbaum A et al., “Frequency of local recurrence following segmentectomy of stage IA non-small cell lung cancer is influenced by segment locatisation and width of resection margins - implications for patient selection for segmentectomy,” European Journal of Cardio-Thoracic Surgery, 31(3), 522–527 (2007). [PubMed: 17229574]

[9]. Karni T, Pappo I, Sandbank J et al., “A device for real-time, intraoperative margin assessment in breastconservation surgery,” American Journal of Surgery, 194(4), 467–473 (2007). [PubMed: 17826057]

[10]. Neoptolemos JP, Stocken DD, Dunn JA et al., “Influence of resection margins on survival for patients with pancreatic cancer treated by adjuvant chemoradiation and/or chemotherapy in the ESPAC-1 randomized controlled trial,” Annals of Surgery, 234(6), 758–768 (2001). [PubMed: 11729382]

[11]. Keereweer S, Kerrebijn JF, Driel PAA et al., “Optical Image-guided Surgery—Where Do We Stand?,” Molecular Imaging and Biology, 13(2), 199–207 (2011). [PubMed: 20617389]

[12]. Nguyen QT, Olson ES, Aguilera TA et al., “Surgery with molecular fluorescence imaging using activatable cell-penetrating peptides decreases residual cancer and improves survival,” Proceedings of the National Academy of Sciences, 107(9), 4317–4322 (2010).

[13]. Meier JD, Oliver DA, and Varvares MA, “Surgical margin determination in head and neck oncology: current clinical practice. The results of an International American Head and Neck Society Member Survey,” Head Neck, 27(11), 952–8 (2005). [PubMed: 16127669]

[14]. Gandour-Edwards RF, Donald PJ, and Wiese DA, “Accuracy of intraoperative frozen section diagnosis in head and neck surgery: experience at a university medical center,” Head Neck, 15(1), 33–8 (1993). [PubMed: 8416854]

[15]. Warram JM, de Boer E, Moore LS et al., “A ratiometric threshold for determining presence of cancer during fluorescence-guided surgery,” J Surg Oncol, 112(1), 2–8 (2015). [PubMed: 26074273]

[16]. Rosenthal EL, Warram JM, de Boer E et al., “Safety and Tumor Specificity of Cetuximab-IRDye800 for Surgical Navigation in Head and Neck Cancer,” Clin Cancer Res, 21(16), 3658–66 (2015). [PubMed: 25904751]

[17]. Hirche C, Engel H, Kolios L et al., “An experimental study to evaluate the Fluobeam 800 imaging system for fluorescence-guided lymphatic imaging and sentinel node biopsy,” Surg Innov, 20(5), 516–23 (2013). [PubMed: 23275469]

[18]. van der Vorst JR, Schaafsma BE, Verbeek FPR et al., “Intraoperative near-infrared fluorescence imaging of parathyroid adenomas with use of low-dose methylene blue,” Head Neck, 36, 853–858 (2014). [PubMed: 23720199]

[19]. Schaafsma BE, Verbeek FP, Rietbergen DD et al., “Clinical trial of combined radio- and fluorescenceguided sentinel lymph node biopsy in breast cancer,” Br J Surg, 100(8), 1037–44 (2013). [PubMed: 23696463]

[20]. Tummers Q, Hoogstins CES, Peters AAW et al., “The Value of Intraoperative Near-Infrared Fluorescence Imaging Based on Enhanced Permeability and Retention of Indocyanine Green: Feasibility and False-Positives in Ovarian Cancer,” PLoS One, 10, e0129766 (2015). [PubMed: 26110901]

[21]. Rosenthal EL, and Zinn KR, “Putting numbers to fluorescent guided surgery,” Mol Imaging Biol, 15(6), 647–8 (2013). [PubMed: 23836503]

[22]. Wolfe WL, “Introduction to imaging spectrometers,” SPIE Press, (1997).

[23]. Goetz AFH, “Three decades of hyperspectral remote sensing of the Earth: A personal view,” Remote Sensing of Environment, 113, Supplement 1, S5–S16 (2009).

[24]. Fischer C, and Kakoulli I, “Multispectral and hyperspectral imaging technologies in conservation: current research and potential applications,” Studies in Conservation, 51, 3–16 (2006).

[25]. Lefei Z, Liangpei Z, Dacheng T et al., “On Combining Multiple Features for Hyperspectral Remote Sensing Image Classification,” IEEE Transactions on Geoscience and Remote Sensing, 50, 879–893 (2012).

[26]. Govender M, Chetty K, and Bulcock H, “A review of hyperspectral remote sensing and its application in vegetation and water resource studies,” Water SA, 33, 145–151 (2007).

[27]. Adam E, Mutanga O, and Rugege D, “Multispectral and hyperspectral remote sensing for identification and mapping of wetland vegetation: a review,” Wetlands Ecology and Management, 18(3), 281–296 (2010).

[28]. Gowen AA, O’Donnell CP, Cullen PJ et al., “Hyperspectral imaging – an emerging process analytical tool for food quality and safety control,” Trends in Food Science & Technology, 18(12), 590–598 (2007).

[29]. Feng YZ, and Sun DW, “Application of hyperspectral imaging in food safety inspection and control: a review,” Crit Rev Food Sci Nutr, 52(11), 1039–58 (2012). [PubMed: 22823350]

[30]. Edelman GJ, Gaston E, van Leeuwen TG et al., “Hyperspectral imaging for non-contact analysis of forensic traces,” Forensic Science International, 223(1–3), 28–39 (2012). [PubMed: 23088824]

[31]. Malkoff DB, and Oliver WR, “Hyperspectral imaging applied to forensic medicine.” Proc. SPIE, 3920, 108116 (2010).

[32]. Kuula J, Pölönen I, Puupponen H-H et al., “Using VIS/NIR and IR spectral cameras for detecting and separating crime scene details.” Proc. SPIE, 8359, 83590P (2012).

[33]. Schuler RL, Kish PE, and Plese CA, “Preliminary Observations on the Ability of Hyperspectral Imaging to Provide Detection and Visualization of Bloodstain Patterns on Black Fabrics,” Journal of Forensic Sciences, 57(6), 1562–1569 (2012). [PubMed: 22563710]

[34]. Carrasco O, Gomez RB, Chainani A et al., “Hyperspectral imaging applied to medical diagnoses and food safety.” Proc. SPIE, 5097, 215–221 (2003)

[35]. Afromowitz MA, Callis JB, Heimbach DM et al., “Multispectral imaging of burn wounds: a new clinical instrument for evaluating burn depth,” Biomedical Engineering, IEEE Transactions on, 35(10), 842–850 (1988).

[36]. Zonios G, Perelman LT, Backman V et al., “Diffuse Reflectance Spectroscopy of Human Adenomatous Colon Polyps In Vivo,” Applied Optics, 38(31), 6628–6637 (1999). [PubMed: 18324198]

[37]. Wang LV, and Wu H-I, “Biomedical Optics: Principles and Imaging,” John Wiley & Sons, Inc., (2009).

[38]. Costas B, Christos P, and George E, “Multi/Hyper-Spectral Imaging,” CRC Press, (2011).

[39]. Tuchin VV, and Tuchin V, “Tissue optics: light scattering methods and instruments for medical diagnosis,” SPIE press Bellingham, (2007).

[40]. Ferris DG, Lawhead RA, Dickman ED et al., “Multimodal Hyperspectral Imaging for the Noninvasive Diagnosis of Cervical Neoplasia,” Journal of Lower Genital Tract Disease, 5(2), 65–72 (2001). [PubMed: 17043578]

[41]. Pierce MC, Schwarz RA, Bhattar VS et al., “Accuracy of In Vivo Multimodal Optical Imaging for Detection of Oral Neoplasia,” Cancer Prevention Research, 5(6), 801–809 (2012). [PubMed: 22551901]

[42]. Lu G, and Fei B, “Medical hyperspectral imaging: a review,” J Biomed Opt, 19(1), 10901 (2014). [PubMed: 24441941]

[43]. Lu G, Halig L, Wang D et al., “Spectral-spatial classification using tensor modeling for cancer detection with hyperspectral imaging.” Proc. SPIE, 9034, 903413 (2014).

[44]. Lu G, Halig L, Wang D et al., “Hyperspectral imaging for cancer surgical margin delineation: registration of hyperspectral and histological images.” Proc. SPIE, 9036, 90360S (2014).

[45]. Halig LV, Wang D, Wang AY et al., “Biodistribution Study of Nanoparticle Encapsulated Photodynamic Therapy Drugs Using Multispectral Imaging,” Proc SPIE, 8672, 867218 (2013).

[46]. Hellebust A, Rosbach K, Wu JK et al., “Vital-dye-enhanced multimodal imaging of neoplastic progression in a mouse model of oral carcinogenesis,” J Biomed Opt, 18(12), 126017 (2013). [PubMed: 24362926]

[47]. Lu G, Wang D, Qin X et al., “Framework for hyperspectral image processing and quantification for cancer detection during animal tumor surgery,” J Biomed Opt, 20(12), 126012 (2015). [PubMed: 26720879]

[48]. Tin Kam H, “The random subspace method for constructing decision forests,” IEEE Transactions on Pattern Analysis and Machine Intelligence, 20(8), 832–844 (1998).

[49]. Luo Z, Loja MN, Farwell DG et al., “Widefield Optical Imaging of Changes in Uptake of Glucose and Tissue Extracellular pH in Head and Neck Cancer,” Cancer Prevention Research, 7(10), 1035–1044 (2014). [PubMed: 25139295]

[50]. Vila P, Park C, Pierce M et al., “Discrimination of Benign and Neoplastic Mucosa with a High-Resolution Microendoscope (HRME) in Head and Neck Cancer,” Annals of Surgical Oncology, 19(11), 3534–3539 (2012). [PubMed: 22492225]

[51]. Lu G, Halig L, Wang D et al., “Spectral-spatial classification for noninvasive cancer detection using hyperspectral imaging,” J Biomed Opt, 19(10), 106004 (2014). [PubMed: 25277147]

[52]. Lu G, Qin X, Wang D et al., “Hyperspectral Imaging of Neoplastic Progression in a Mouse Model of Oral Carcinogenesis,” Proc. SPIE, 9791, 978812 (2016).

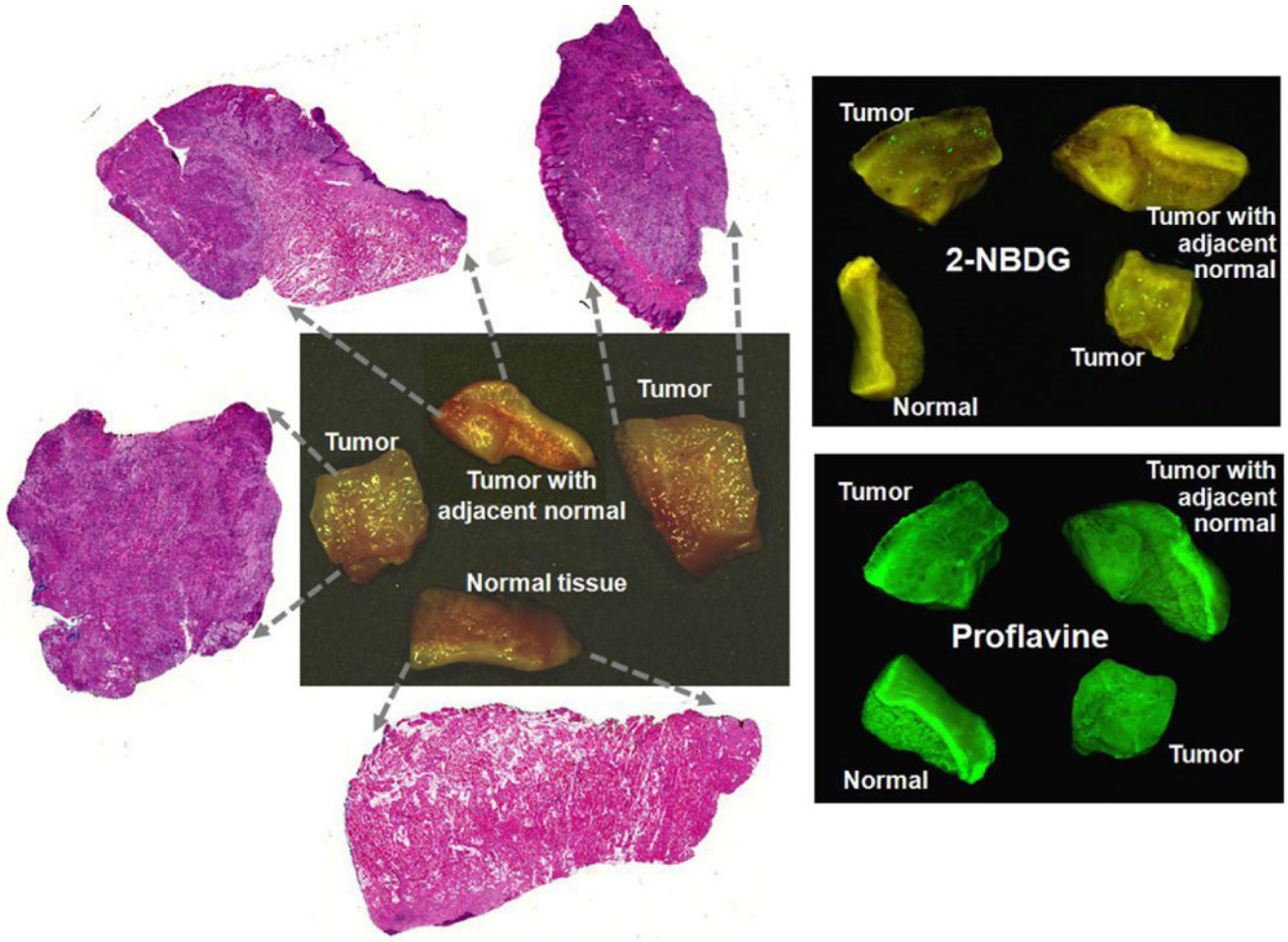

Figure 1.
Surgical specimens of tumor, normal tissue, and tumor with adjacent normal tissue from a tong cancer patient. *Left:* Tissue and corresponding histological slides. *Right:* 2-NBDG and Proflavine fluorescence images for each tissue.

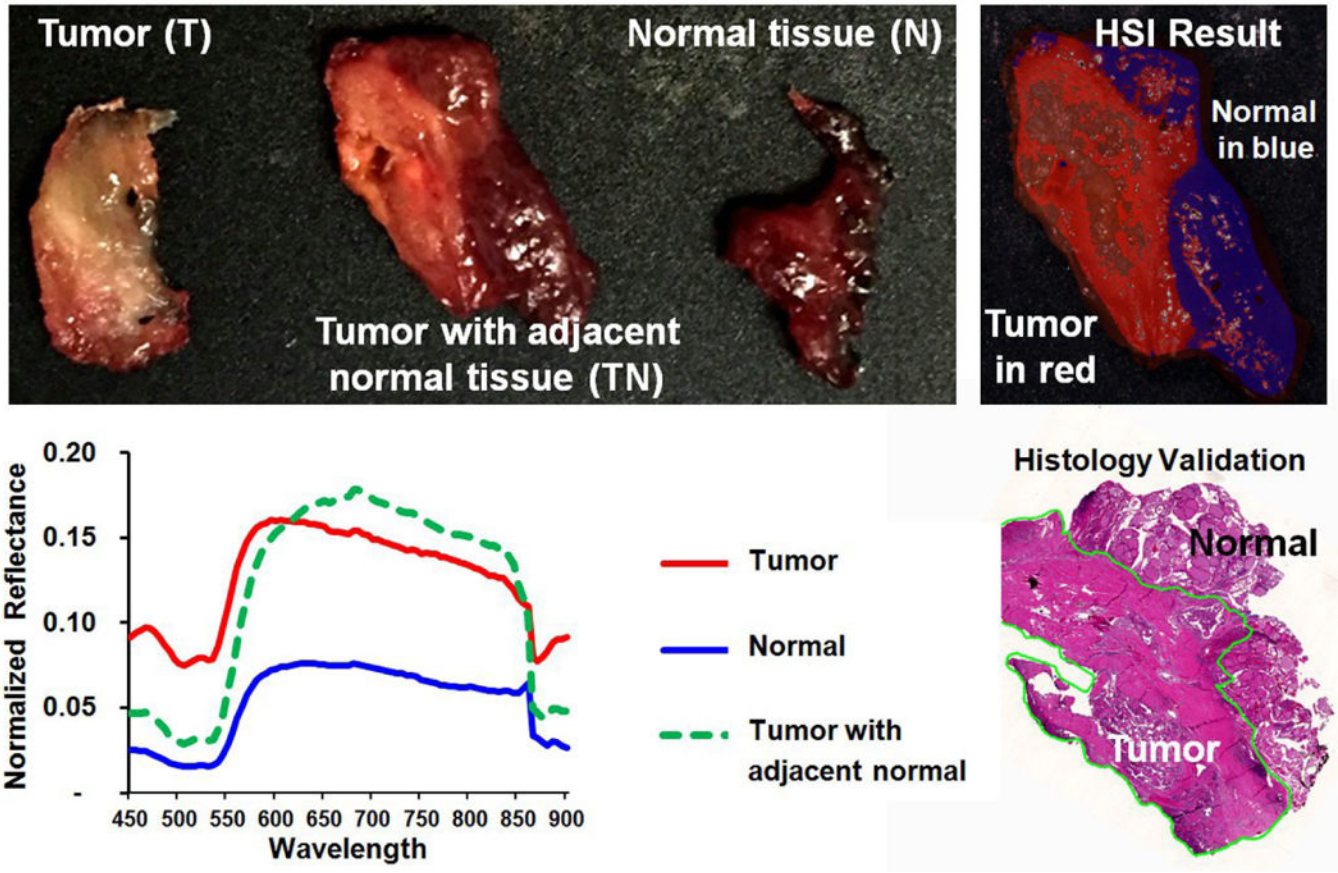

Figure 2.

Tumor margin detection of surgical specimens from an H&N cancer patient. After hyperspectral image acquisitions, the tissue were processed histologically and tumor margins were outlined on the pathologic image (bottom right) by a pathologist (JVL), which was used to validate the results of the classification (top-right). The average spectral curves are shown at the bottom left for each type of tissue (tumor, normal, and tumor with adjacent normal tissue).

Table 1.

Classification performance of HSI, autofluorescence imaging, and fluorescence imaging with 2-NBDG and proflavine.

Cancer Site	Imaging Method	AUC	Accuracy	Sensitivity	Specificity
Oral Cavity	HSI	0.94±0.06	90%±8%	89%±9%	91%±6%
	Autofluorescence	0.83±0.19	80%±18%	78%±21%	86%±14%
	2-NBDG	0.86±0.16	83%±15%	81%±19%	85%±11%
	Proflavine	0.72±0.25	70%±21%	71%±20%	70%±22%
Thyroid	HSI	0.98±0.03	94%±6%	94%±6%	95%±6%
	Autofluorescence	0.74±0.33	70%±34%	76%±23%	77%±35%
	2-NBDG	0.80±0.20	76%±20%	75%±22%	79%±19%
	Proflavine	0.86±0.16	82%±16%	79%±18%	85%±13%